Earth Planet. Sci. Lett. 673 (2026) 119716

Contents lists available at ScienceDirect

Earth and Planetary Science Letters

journal homepage: www.elsevier.com/locate/epsl

P and S wave finite-frequency tomography reveals the impact of slab interference on mantle flow beneath the greater Alpine region

Yuantong Mao[a], Xiaotian Tang[a], Liang Zhao[b,c,**], Marco G. Malusà[d,*], Stéphane Guillot[e], Anne Paul[e], Stefano Solarino[f], Xiaobing Xu[g], Coralie Aubert[e], Elena Eva[f], Silvia Pondrelli[h], Simone Salimbeni[h], Lei Yang[a,c]

[a] *State Key Laboratory of Lithospheric and Environmental Coevolution, Institute of Geology and Geophysics, Chinese Academy of Sciences, Beijing 100029, China*
[b] *Key Laboratory of Deep Petroleum Intelligent Exploration and Development, Institute of Geology and Geophysics, Chinese Academy of Sciences, Beijing 100029, China*
[c] *College of Earth and Planetary Sciences, University of Chinese Academy of Sciences, Beijing 100049, China*
[d] *Department of Earth and Environmental Sciences, University of Milano-Bicocca, Milan 20126, Italy*
[e] *Université Grenoble Alpes, Université Savoie Mont Blanc, CNRS, IRD, UGE, ISTerre, Grenoble 38000, France*
[f] *Istituto Nazionale di Geofisica e Vulcanologia, Osservatorio Nazionale Terremoti, Genova 16145, Italy*
[g] *Department of Mathematical Sciences, Tsinghua University, Beijing 100084, China*
[h] *Istituto Nazionale di Geofisica e Vulcanologia, Sezione di Bologna, Bologna 40127, Italy*

ARTICLE INFO

Editor: Dr H Thybo

Keywords:
P- and S-wave imaging
Upper mantle
Greater alpine region
Slab interference
Mantle flow
Finite-frequency Tomography

ABSTRACT

The Cenozoic evolution of the tortuous Adria-Europe plate boundary zone suggests potential interference between opposite-dipping slabs in the upper mantle, with potential perturbation of the surrounding mantle flow. However, compelling seismic evidence of slab interference beneath the greater Alpine region is still lacking. Here we use P- and S-wave velocity models based on the Finite-Frequency Tomography method to reveal the interactions between slabs imaged beneath the greater Alpine region and their relationships with prominent low-velocity anomalies in the upper mantle. We document high-velocity anomalies beneath the Alps, the Apennines and the northern Dinarides. A velocity gap is imaged between the Alpine and Apenninic slabs. Low-velocity anomalies are found to the west of the Alps, beneath the Po Plain, and on either side of the central-southern Apennines. Because of slab interference, low-velocity anomalies of different origins, either due to asthenospheric upwelling or slab fluids, coexist in nearby regions of the upper mantle. The lack of major gaps between the Western Alpine slab and the retreating Apennine slab makes a potential toroidal flow around the northern tip of the Apennine slab during slab rollback difficult, with consequent activation of an asthenospheric counterflow and associated mantle upwelling to the west of the Alps. Beneath the Eastern Alps, the Alpine slab is torn and overturned by the NE-dipping Dinaric slab. The asthenospheric mantle beneath the Po Plain is confined by slabs and shows a prominent low-velocity anomaly likely due to melting triggered by carbon-rich supercritical fluids generated above the Alpine slab. Toroidal flow may occur farther south around the Apenninic slab, in a region where the mantle flow is not affected by interaction between slabs. Similar complexities may characterize other plate-boundary zones where the interplay between opposite-dipping slabs is suggested by geophysical and geological data, such as the Taiwan orogeny or the Hindu Kush - Pamir - Tianshan tectonic knot in Central Asia.

1. Introduction

The greater Alpine region has been shaped by the convergence of the European plate and the Adriatic microplate from the Cretaceous to the present (Dewey et al., 1989; Jolivet and Faccenna, 2000; Handy et al., 2010; Malusà et al., 2015). It includes several orogenic belts, such as the Alps, the Apennines and the Dinarides (Fig. 1), which overlie a complex and still-debated slab structure (e.g., Lippitsch et al., 2003; Piromallo and Morelli, 2003; Koulakov et al., 2009; Giacomuzzi et al., 2011; Zhao et al., 2016a; Paffrath et al., 2021; Rappisi et al., 2022; Kästle et al.,

---

* Corresponding author.
** Corresponding author at: Key Laboratory of Deep Petroleum Intelligent Exploration and Development, Institute of Geology and Geophysics, Chinese Academy of Sciences, Beijing 100029, China.
E-mail addresses: zhaoliang@mail.iggcas.ac.cn (L. Zhao), marco.malusa@unimib.it (M.G. Malusà).

https://doi.org/10.1016/j.epsl.2025.119716
Received 7 March 2025; Received in revised form 17 October 2025; Accepted 2 November 2025

2025). These slabs are thought to control the flow pattern in the surrounding asthenospheric mantle (Barruol et al., 2004; Vignaroli et al., 2008; Jolivet et al., 2009; Baccheschi et al., 2024), which in turn significantly influences the topography of the region (Faccenna and Becker, 2010; Salimbeni et al., 2018; Sternai et al., 2019).

The geologic evolution of the Adria-Europe plate boundary zone, which is characterized by a prolonged northward motion of Adria relative to Europe (Fig. 1a), supports the hypothesis of slab interference at depth, which is expected to affect the surrounding mantle flow. However, compelling seismic evidence of slab interference is still lacking, and would require higher-resolution seismic tomography models. Based on available geological constraints, regions of potential slab interaction are located in the Alps-Apennines transition zone, where interaction between the Western Alps slab and the retreating Apenninic slab may have controlled the location of the rotation pole of the Corsica-Sardinia block (Gattacceca et al., 2007; Malusà et al., 2016), and in the transition zone between the Eastern Alps and the Dinarides, where the northward motion of the Dinaric slab may have induced tearing of the Alpine slab (Ji et al., 2019; Mosconi et al., 2024). The integration of geophysical imaging and petrological modeling has revealed large-scale carbon processes in these regions of slab interaction (Malusà et al., 2018), with a major carbon reservoir, formed in the Adriatic upper mantle during Alpine subduction, partially remobilized by anomalously deep earthquakes (Eva et al., 2020; Malusà et al., 2022). Other tomographic studies have documented a subduction polarity reversal from the Central Alps to the Eastern Alps (Zhao et al., 2016a; Kästle et al., 2020; Paffrath et al., 2021), but the European vs. Adriatic origin of the slab beneath the Eastern Alps remains unclear (Koulakov et al., 2009; Malusà et al., 2021; Jozi Najafabadi et al., 2022).

To shed light on these issues, here we present a higher-resolution teleseismic P-wave finite-frequency tomography model and an S-wave tomography model of the Alpine region, based on previously unused, denser seismic datasets from permanent networks and temporary stations of the AlpArray (Hetenyi et al., 2018) and CIFALPS and CIFALPS2 (Zhao et al., 2016b, 2018) seismic experiments. For crustal corrections, we utilized the new AlpsLig-crust_WET model, which has a crustal resolution of 0.02° and was derived from ambient-noise wave-equation tomography (Nouibat et al., 2023). Our results provide unprecedented evidence of slab interactions beneath the greater Alpine region, which we discuss in terms of their impact on asthenospheric mantle flow and

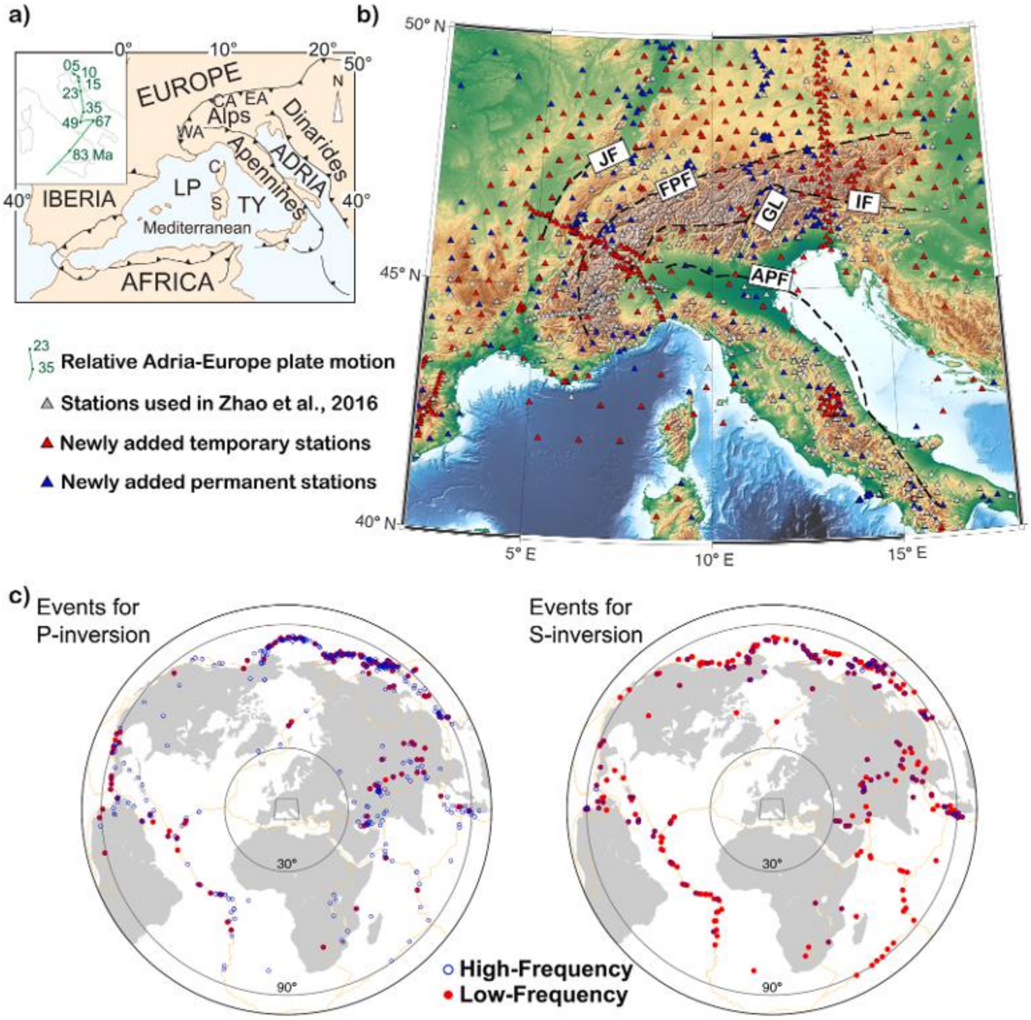

Fig. 1. Tectonic setting, seismic stations and event distribution for P and S wave finite-frequency tomography. (a) Tectonic sketch map of the study area and relative motion of the Adriatic microplate relative to Europe since the Late Cretaceous (after Dewey et al., 1989; Jolivet and Faccenna, 2000). Acronyms: WA, Western Alps; CA, Central Alps; EA, Eastern Alps; C, Corsica; S, Sardinia; LP, Ligurian-Provençal Basin; TY, Tyrrhenian Basin. **(b)** Seismic station distribution on topography map. The gray triangles indicate stations from previous studies (Zhao et al., 2016a), the red and blue triangles indicate the newly added temporary and permanent stations of this study. Main tectonic boundaries (black dashed lines): FPF, Frontal Pennine Fault; APF, Apennines Front; IF, Insubric Fault; GL, Giudicarie Line; JF, Jura Front. **(c)** Events distribution for P- and S-wave inversion used in this study. The blue circles denote the selected events of high frequency (P: 0.5∼2 Hz, S: 0.1∼0.5 Hz), the red dots denote selected events of low frequency (P: 0.1∼0.5 Hz, S: 0.05∼0.1 Hz). The brown lines indicate major plate boundaries. The gray rectangle marks the study area.

associated geologic process in the upper mantle, with potential applications to other complex plate-boundary zones worldwide.

2. Data and methods

2.1. Data selection and analysis

The seismic datasets used in this study were collected from 1093 seismic stations deployed in the greater Alpine area from 2012 to 2020 (Fig. 1b). Compared to the tomography conducted by Zhao et al. (2016a), this study utilized nearly twice as many seismic stations, which include 659 permanent stations collected from the European Integrated Data Archive (EIDA) European archive (http://webdc.eu/webdc3/), 110 temporary broadband seismic stations from the dense arrays of the CIFALPS seismic experiments across the southern and northern Western Alps (Zhao et al., 2016b, 2018), and 324 temporary stations from the AlpArray Seismic Network across the Alpine region (Hetenyi et al., 2018). As shown in Fig. 1b, both the Alps and the Apennines are well covered by seismic stations, although not all stations remained operational throughout the study period, and only the Tyrrhenian Sea, the Adriatic Sea and the southern Dinarides have lower coverage. Within this framework, the availability of abundant seismic data enabled the selection of not only high-quality P-wave travel time residuals but also S-wave travel time residuals for tomography.

Using CrazySeismic (Yu et al., 2017), we measured the travel time residuals with respect to synthetic arrival times derived from the IASPEI91 1D velocity model (Kennett and Engdahl, 1991), an open-source software package that employs multi-channel cross-correlation (VanDecar and Crosson, 1990). Finite frequency theory postulates that seismic waveforms with different frequencies are sensitive to velocity anomalies of different scales (Dahlen et al., 2000; Hung et al., 2000), where lower-frequency waveforms are sensitive to larger-scale structures, whereas higher-frequency waveforms being sensitive to smaller-scale structures. In this study, two different frequency bands were selected for both P and S waves, that is 0.1–0.5 Hz and 0.5–2 Hz for P waves, and 0.05–0.1 Hz and 0.1–0.5 Hz for S waves. To ensure data quality for tomography, the following three criteria were applied in event selection and travel time residual measurements: (1) selected teleseismic events have magnitude > 5 and epicentral distances between 30° and 90°; (2) each selected event is recorded by a minimum of 50 stations and includes high-quality waveforms from the reference station DAVOX, to ensure that the relative travel time residuals reflect variations in velocity anomalies rather than inconsistencies due to uneven station recording over a long-time interval; (3) relative travel time is less than three standard deviations of the total dataset. The number of seismic events and travel time residuals selected for inversion across different frequency Nbands are listed in Supplementary Table S1. In total, 217,809 P-waveforms and 104,817 S-waveforms were collected, resulting in a substantial dataset. The distribution of events is shown in Fig. 1c. Examples of selected waveforms are shown in Supplementary Figs. S1 and S2.

We analyzed travel time residuals for seismic events across multiple back-azimuths (Supplementary Fig. S3). Residuals for both P and S waves exhibit a consistent pattern. The region extending from the southern Western Alps to the French Central Massif is characterized by late arrivals, whereas the foreland area northwest of the Western Alps shows early arrivals. The relative travel time residuals vary with ray azimuths, highlighting lateral heterogeneity in the crust and upper mantle.

2.2. Crustal correction

Previous studies have already demonstrated that the Alpine region is characterized by significant velocity heterogeneities in the upper crust and the mantle (Zhao et al., 2015; Kästle et al., 2018; Solarino et al., 2018; Lu et al., 2020; Zhao et al., 2020; Monna et al., 2022; Nouibat et al., 2022; Paul et al., 2022; Kind et al., 2023; Nouibat et al., 2023; Solarino et al., 2024; Mao et al., 2024). In this teleseismic tomography study, to account for the crustal heterogeneity affecting S waves, we utilized the AlpsLig-crust_WET model, which has a crustal resolution of 0.02° and was derived from ambient-noise wave-equation tomography (Nouibat et al., 2023). For regions outside the coverage of the AlpsLig-crust_WET model, the Eucrust_transD-ANT model was alternatively employed, with a resolution of 0.15° (Nouibat et al., 2022). High-resolution P-wave velocity crustal structures are typically derived from local earthquake tomography (Solarino et al., 2018; Jozi Najafabadi et al., 2022, 2024). However, due to the heterogeneous distribution of intermediate depth earthquakes in the Alpine region (e.g., Eva et al., 2020), the availability of crustal models based on the analysis of P waves is limited. Therefore, we used the S-wave crustal velocity model scaled by a factor of 1.73 for P-wave crustal correction. The scaling factor of 1.73 follows conventional crustal Vp/Vs ratios. Comparative tests using S-wave-based P-wave velocity models with empirical relationships (Brocher, 2005) produced indistinguishable imaging results (Supplementary Fig. S4). We employed a 1D ray tracing algorithm to calculate crustal residuals beneath all stations, focusing on the crust and the uppermost mantle above 50 km depth, which were subsequently subtracted from the teleseismic travel time residuals. The crustal travel time residuals are shown in Supplementary Fig. S5. Orogenic belts generally exhibit travel time delays, while regions in the foreland, particularly the so-called Ivrea Body (at 7.5–8°E) (Closs and Labrouste, 1963), display travel time advances, suggesting that crustal correction may lead to more reliable imaging of the underlying upper mantle. After applying the refined velocity model for crustal correction, the imaging results exhibit significant modifications, especially in the uppermost mantle beneath mountain belts. The P-wave and S-wave velocity images before and after crustal correction are presented in Supplementary Figs. S6 and S7, and show continuous high-velocity anomalies that become more pronounced after crustal correction, particularly at depths above 150 km.

2.3. Finite frequency tomography method

We employed the finite-frequency tomography method (Dahlen et al., 2000; Hung et al., 2000) to image the velocity structure of the upper mantle. This approach accounts for the effects of velocity perturbations in the vicinity of the ray path, rather than assuming infinitely high-frequency ray paths, thus providing a more accurate representation of the impact of velocity structure on arrival times. The grid configuration was designed based on our study area. Using 64 grid cells in each dimension (longitude, latitude, and depth) achieves an optimal balance between computational efficiency and resolution requirements. Given the dimensions of our computational domain (16° longitude × 10° latitude × 1600 km depth), this setup results in grid intervals of ~27.8 km in longitude, ~17.5 km in latitude, and ~25 km in depth. Subsequently, separate inversion matrices were formulated for the P-wave and S-wave datasets based on the finite-frequency kernel formulation. We applied the damped LSQR (Paige and Saunders, 1982) method to determine the damping factor by balancing the trade-off between the model norm and variance reduction. The damping factors used in this study, 100 for P waves and 140 for S waves, yield a variance reduction of approximately 85 % for the P-wave model and 74 % for the S-wave model (Supplementary Fig. S8).

2.4. Resolution model

We conducted checkerboard tests to assess model resolution by reconstructing synthetic models with known alternating high- and low-velocity anomalies, using the same source-receiver geometry as the actual data inversion. To simulate noise, 10 % Gaussian white noise was added to the synthetic travel time residuals. Several checkerboard scales were examined, with $4 \times 4 \times 4$ (~110 km × 70 km × 100 km) and 5×5

× 5 (~139 km × 88 km × 125 km) grids ultimately chosen as optimal resolutions for P waves and S waves, respectively. The synthetic model configurations incorporated ±3 % anomalies for P waves and ±5 % anomalies for S waves. Synthetic arrival times were generated for the same event-station pairs as the observed data, and the resulting models were evaluated to determine upper mantle resolution. The recovery models exhibit robust resolution for both P-wave and S-wave datasets, particularly in the Alps (Supplementary Figs. S9–S12). Some regions exhibit reduced velocity anomaly amplitudes in the checkerboard tests due to limited data coverage and the use of damping parameters in the inversion process, which is a common issue in seismic tomography studies (Lévêque et al., 1993; Rawlinson and Sambridge, 2003). In our

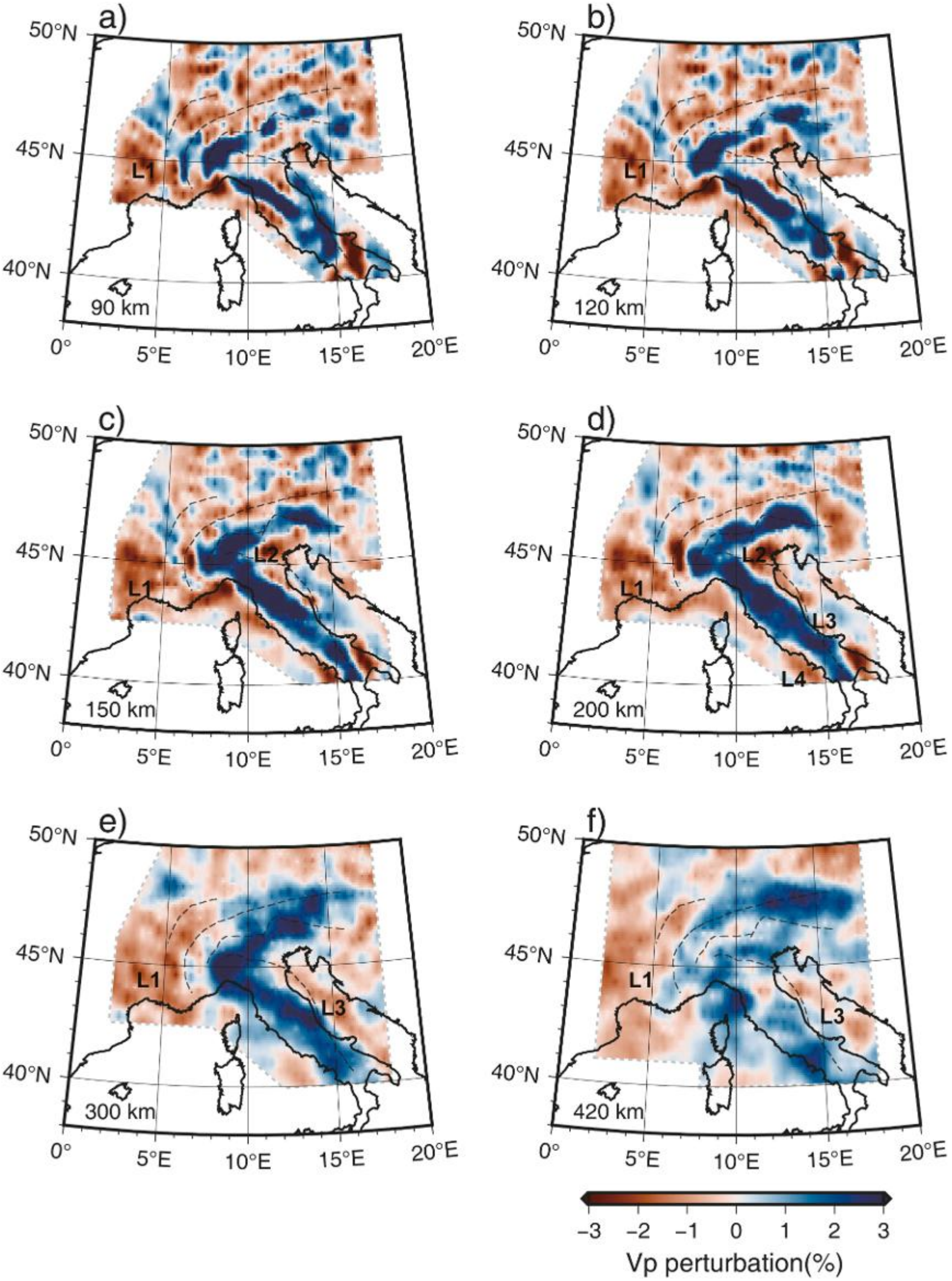

Fig. 2. Depth slices of the P-wave velocity perturbation model at different depths. The gray dashed lines mark the outlines of the well-resolved areas estimated from resolution tests (Figure S9). Main tectonic boundaries (grey dashed lines) as in Fig. 1b L1 to L4 indicate the main low-velocity anomalies discussed in the text.

results, a recovery accuracy of 2 % for P waves and 3 % for S waves is considered indicative of good resolution.

P waves, with their higher frequencies compared to S waves, are more effective at detecting smaller anomalies and offer better resolution. Beneath the Alps, the P-wave dataset adequately resolves the velocity structure in the uppermost 600 km. In contrast, S waves are more sensitive to larger anomalies in the uppermost 400 km. Beneath the Apennines, resolution is spatially limited due to insufficient ray coverage. Only results from regions with sufficient resolution are discussed in the next sections. Smearing effects are visible in both the depth slices and cross-sections, influenced by the preferential directions of seismic rays. Additional synthetic tests could help distinguish whether the observed inclined structures in cross-sections are due to the actual velocity structure or the uneven distribution of seismic rays. Therefore, we performed synthetic tests to further evaluate the model's ability to resolve gaps between slabs, which are described in Sect. 4.1.

3. Results

3.1. *Main features of the P and S wave tomography models*

Figs. 2 and 3 present the updated high-resolution perturbation velocity model for P waves, whereas Figs. 4 and 5 illustrate the newly developed perturbation velocity model for S waves. The P-wave tomography model is based on a more extensive dataset than previous models and includes updated crustal corrections. In the horizontal depth slices of Fig. 2 are evident the high-velocity anomalies beneath the Alps, the Apennines and the northern Dinarides. Prominent low-velocity anomalies are observed to the west of the Alps (L1), beneath the Po Plain (L2), and on either side of the high-velocity anomaly beneath the central-southern Apennines (L3 and L4) (Fig. 2). The S-wave velocity model reveals similar high-velocity features, with the strongest anomalies beneath the Alps and northern Apennines, and low-velocity anomalies L1 to L4 that are particularly prominent (Fig. 4). The high-velocity anomaly beneath the Apennines shows a gap at shallow depth in the S-wave tomography model at ~13.5°E (Fig. 3b). Five cross-sections A-A' to E-E' (Figs. 3, 5) traverse the high- and low-velocity anomalies detected in map view in the P- and S-wave tomography models to investigate their spatial relationships.

The cross-section A-A' traverses the Western Alps and the northernmost Apennines, reaching the eastern Po Plain (Fig. 3a). It reveals a broad high-velocity anomaly at depths of 150–300 km, which may be indicative of slab interference. Within this anomaly, the P-wave velocity model provides higher-resolution results, identifying a gap that likely reflects the presence of two distinct E-dipping slabs, the Western Alps slab (WA) to the west and the Apenninic slab (AP) to the east. These two slabs are also discernible in the S-wave velocity model (Fig. 5a). In both models, the Western Alps slab can be traced continuously to depths greater than 400 km, extending to the mantle transition zone and even deeper. The broad low-velocity anomaly L1, located to the west of the Western Alps (Figs. 3a and 5 a), extends from the mantle transition zone to the uppermost mantle, with particularly high amplitude in the S-wave velocity model (Fig. 5a). To the east, the cross-section A-A' intersects the low-velocity anomaly L2 beneath the Po Plain, which has been attributed by previous work (Malusà et al., 2018, 2022) to carbon-rich melts in the asthenosphere generated by the breakdown of slab carbonates and hydrous minerals after cold subduction. In the S-wave tomography model, this anomaly is particularly evident in the depth range between 300 and 175 km depth (Fig. 5a).

The cross-section B-B' traverses the Central Alps (Fig. 3b) and reveals a SE-dipping high-velocity anomaly, interpreted as the Central Alps slab (CA). This can be traced down to the mantle transition zone and becomes more shallow dipping at ~300 km depth. Above the Central Alps slab lies the low-velocity anomaly L2, which exhibits significant

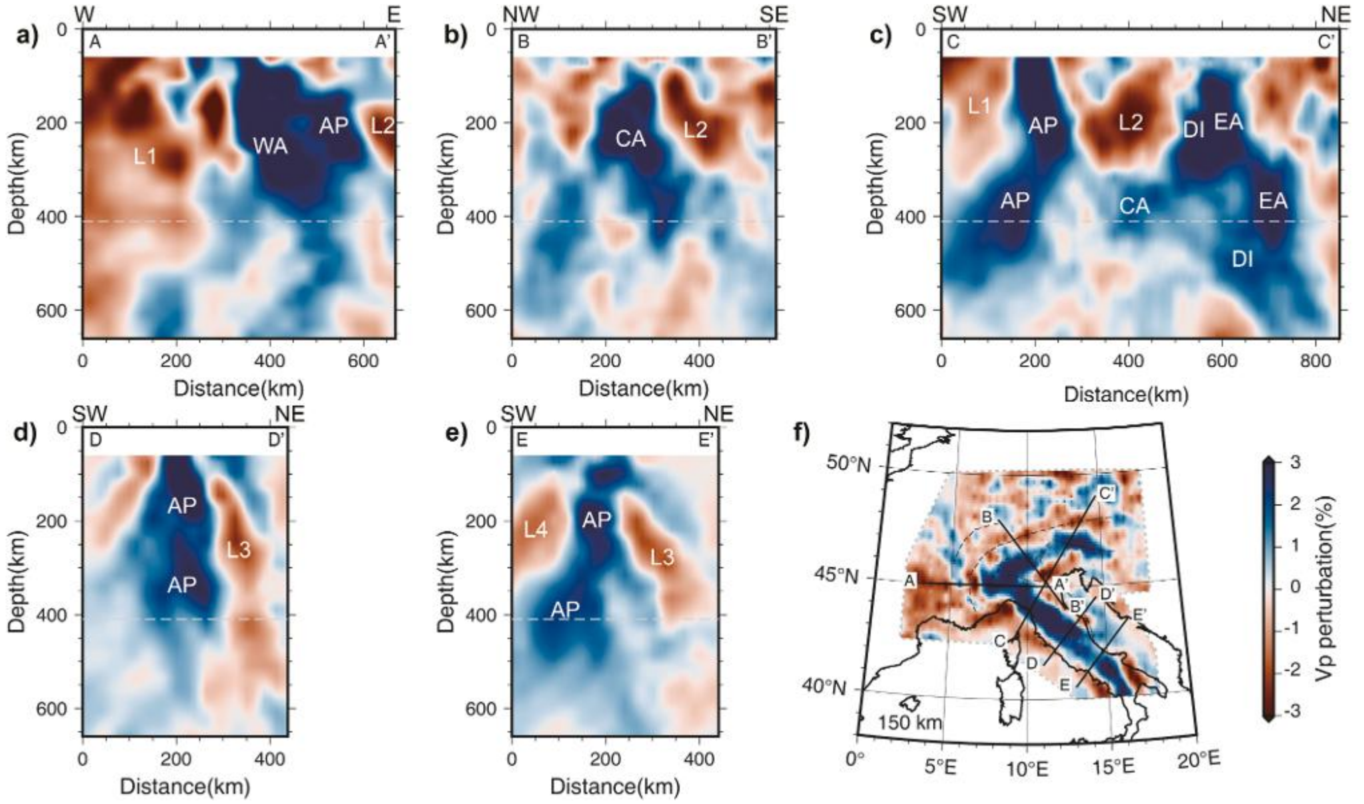

Fig. 3. Cross sections of the P-wave velocity perturbation model (a-e). Cross-section locations are indicated on the 150 km depth slice of the P-wave velocity model **(f)**. High-velocity anomalies are labeled as follows: WA (Western Alps), CA (Central Alps), EA (Eastern Alps), DI (Dinarides), AP (Apennines). L1 to L4 mark the main low-velocity anomalies discussed in the text.

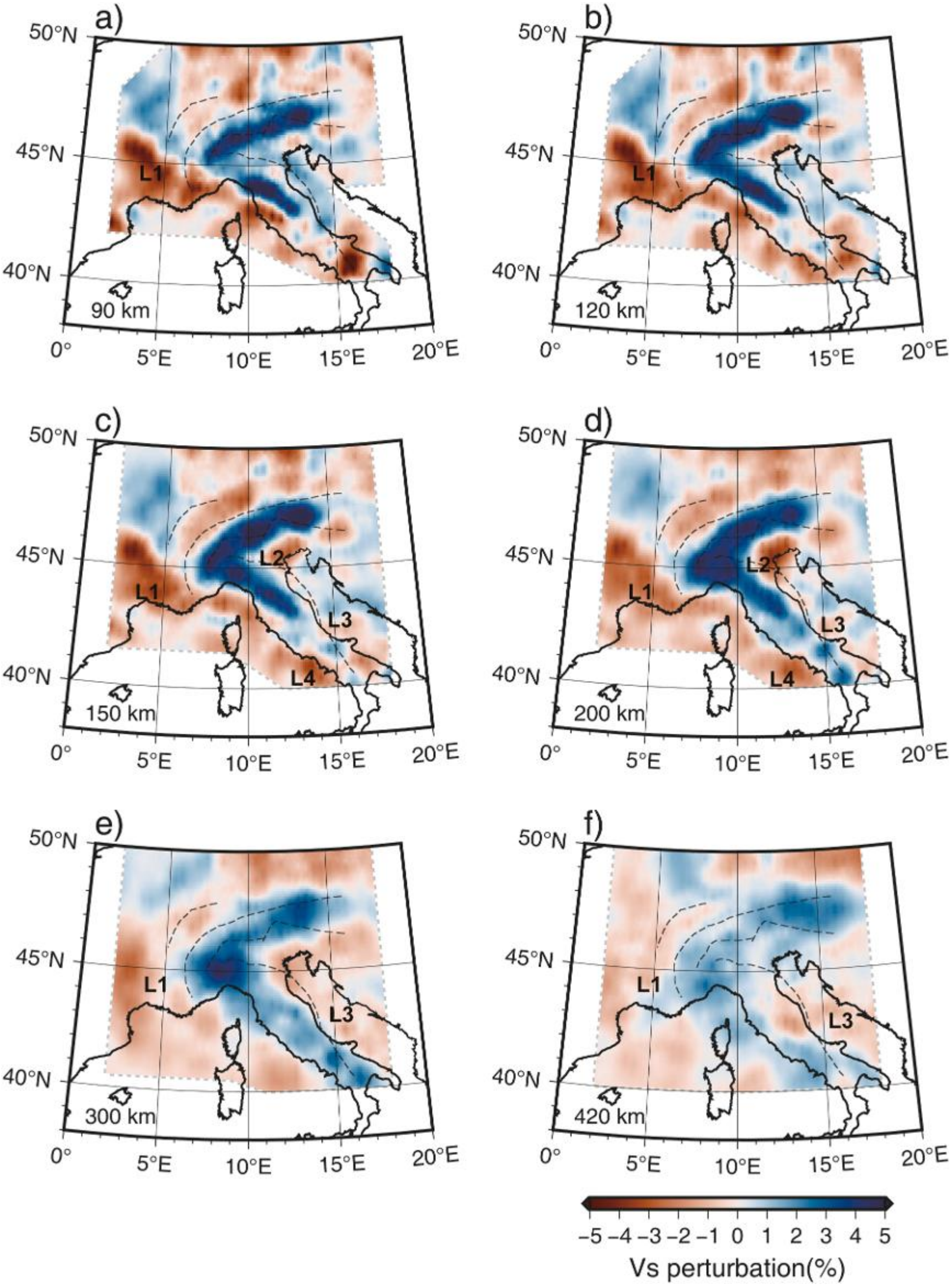

Fig. 4. **Depth slices of the S-wave velocity perturbation model at different depths.** The gray dashed lines mark the outlines of the well-resolved areas estimated from resolution tests (Figure S11). Main tectonic boundaries (grey dashed lines) as in Fig. 1b L1 to L4 indicate the main low-velocity anomalies discussed in the text.

amplitude in both the P-wave and S-wave velocity models (Figs. 3b and 5 b). Its depth is constrained to 150–300 km in the P-wave tomography model (Figs. 3b), and it is prominent in the S-wave tomography model in the depth range between 175 and 300 km.

The cross-section C—C' traverses the Eastern Alps, the Po Plain, and the Northern Apennines (Figs. 3c and 5 c). The high-velocity anomaly observed beneath the Eastern Alps is NE-dipping and extends down to a depth of 600 km. It is notably broad in both the P-wave and S-wave velocity models, suggesting close spacing between interacting slabs. The Eastern Alps slab (EA) lies to the north, while the Dinaric (DI) slab lies to the south. However, they are difficult to distinguish, especially in the S-wave model. To the southwest, beneath the Po Plain, the low-velocity

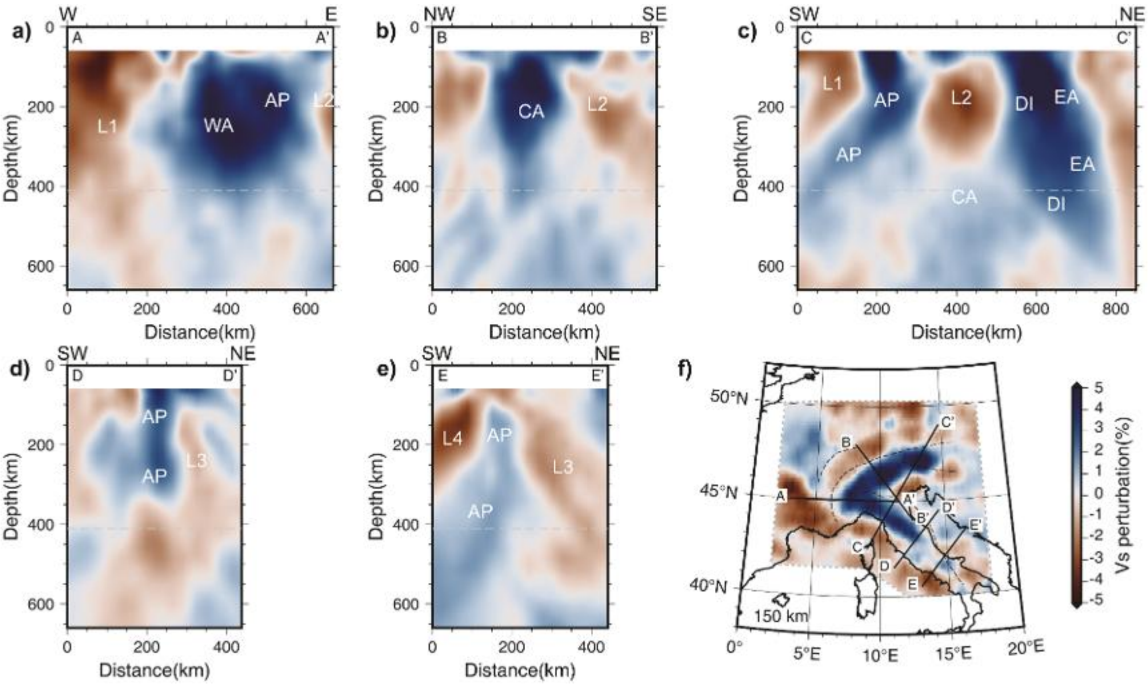

Fig. 5. Cross sections of the S-wave velocity perturbation model (a-e). Cross-section locations are indicated on the 150 km depth slice of the S-wave velocity model **(f)**. High-velocity anomalies are labeled as follows: WA (Western Alps), CA (Central Alps), EA (Eastern Alps), DI (Dinarides), AP (Apennines). L1 to L4 mark the main low-velocity anomalies discussed in the text.

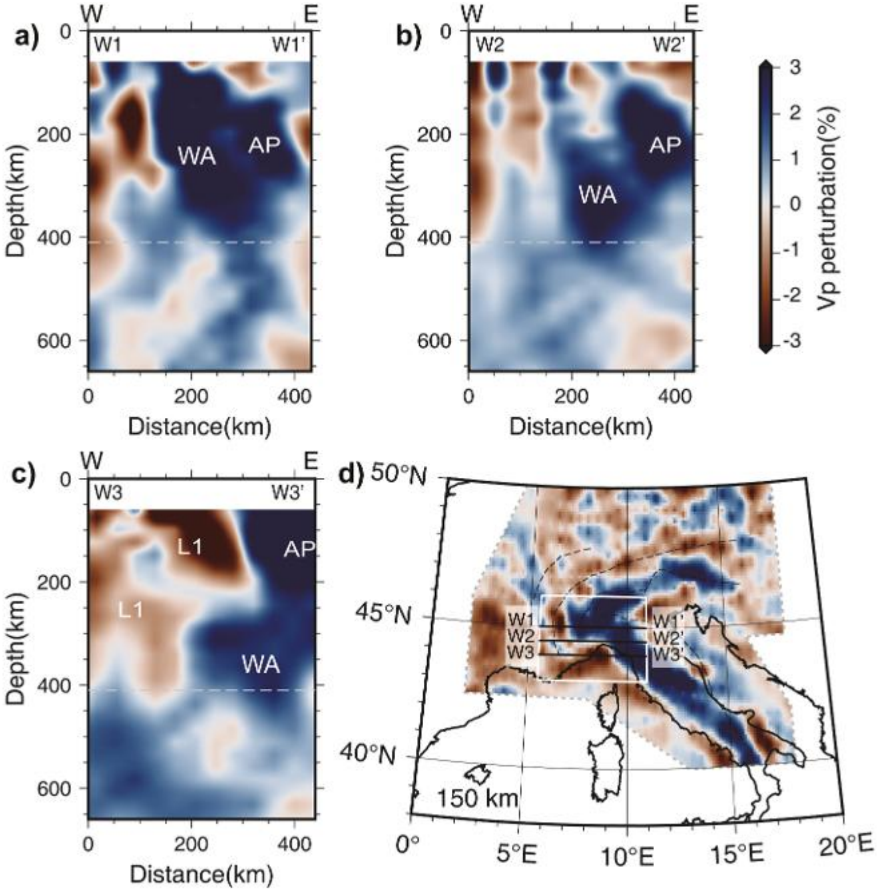

Fig. 6. Cross-sections of the Western Alps - Apennines transition zone. (a-c) P-wave velocity cross sections. **(d)** Cross-section locations on the 150 km depth slice of the P-wave velocity perturbation model. AP: Apennines, WA: Western Alps.

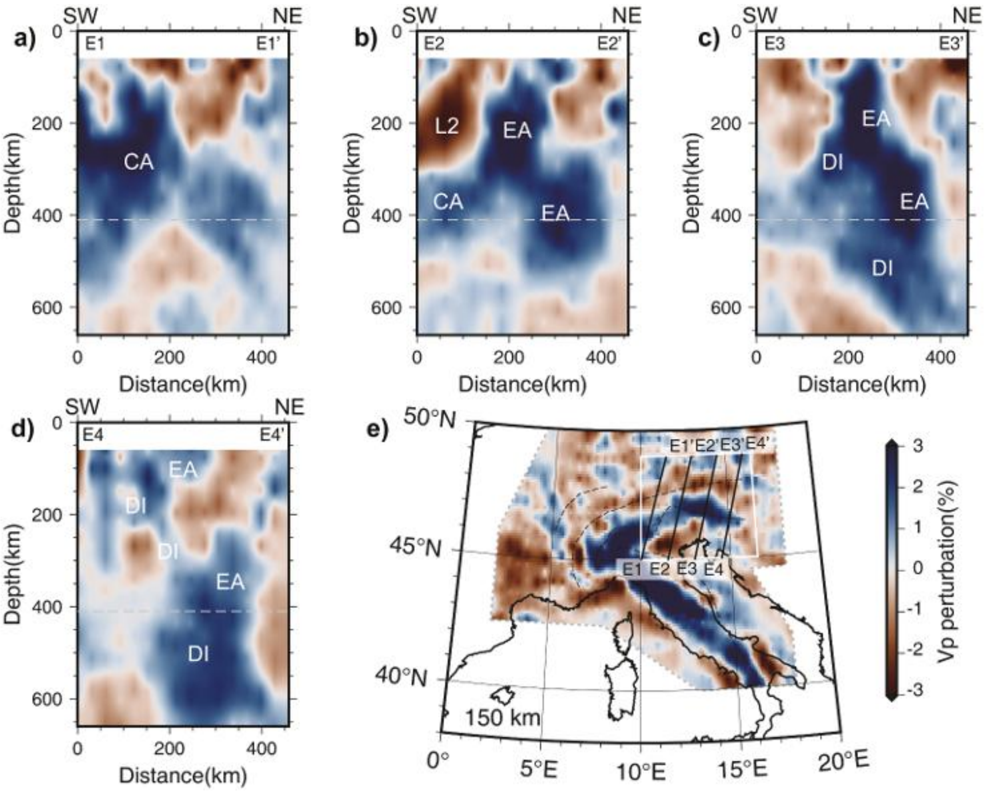

Fig. 7. Cross-sections of the Eastern Alps – Dinarides transition zone. (a-d) P-wave velocity cross sections. **(e)** Cross-section locations on the 150 km depth slice of the P-wave velocity perturbation model. CA: Central Alps, EA: Eastern Alps, DI: Dinarides.

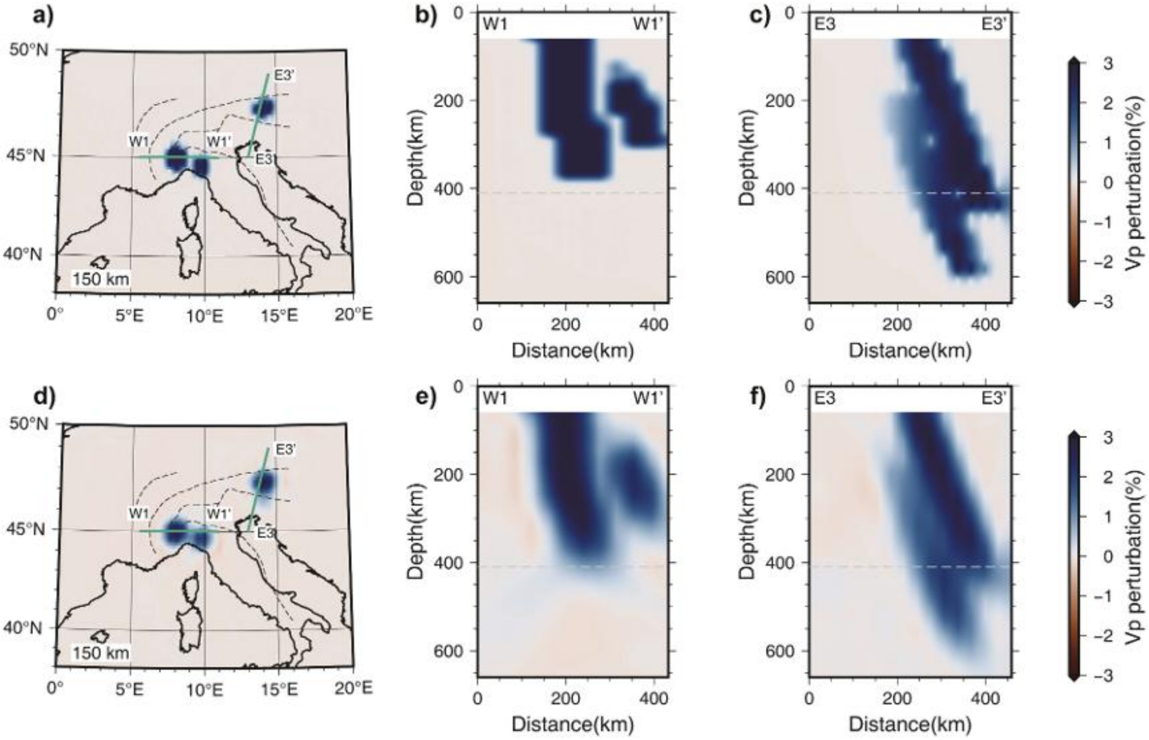

Fig. 8. Resolution analysis of slab interaction. (a-c) The input model includes four high-velocity anomalies with a 3 % increase in P-wave velocity in the upper mantle, designed to represent the slabs of the Western Alps, the Eastern Alps, the Apennines, and the Dinarides. The cross-sections in (b) and (c) correspond to and are labelled as those shown in Figs. 6 and 7. **(d-f)** Recovered velocity models.

anomaly L2 lies above the Central Alps slab (CA). A continuous NE-dipping high-velocity anomaly is observed further southeast beneath the Apennines. It represents the Apenninic (AP) slab, becoming SW-dipping at depths greater than 250 km. Above the high-velocity anomaly of the Apenninic slab lies the low-velocity anomaly L1.

The cross-sections d-D' and E-E' traverse the Apennines parallel to section C—C' (Fig. 3d, e and 5 d, e). They reveal a continuous high-velocity anomaly attributed to the Apenninic slab (AP). The anomaly is near-vertical in cross-section d-D', and SW-dipping in cross section E-E', reaching to depths of 600 km. The slab window, identified in previous studies above 150 km depth beneath the central Apennines (Giacomuzzi et al., 2011; Zhao et al., 2016a), is exclusively observed in the S-wave tomography model along cross-section E-E' (Fig. 5e). Below 150 km depth, however, the high-velocity anomaly remains continuous. Two low-velocity anomalies are detected on either side of the Apenninic slab: the anomaly L3 on the NE side, and the anomaly L4 on the SW side. The anomaly L3 extends below the slab from the mantle transition zone to ~100 km depth, whereas the anomaly L4 extends above the slab and at depth shallower than 300 km. It is weaker along cross-section d-D' than along cross-section E-E' and is apparently disconnected from anomaly L1.

3.2. *Western Alps - Apennines transition zone*

In the transition zone between the Western Alps and the Apennines, our high-resolution velocity model clearly differentiates the Western Alps slab and the Apenninic slab. Fig. 6 illustrates three east-west profiles to further explore the relationship between these two slabs.

In the northernmost profile (Fig. 6a), the cross-section primarily intersects the Western Alps slab, which extends continuously from the Earth's surface down to a depth of at least 400 km. Another high-velocity anomaly, corresponding to the northern tip of the Apenninic slab, is observed to the east of the Western Alps slab at depths of approximately 100–300 km. A velocity gap is evident between the two slabs, marked by a low-amplitude anomaly that highlights their separation. Although the P-wave velocity model offers higher resolution, a similar feature is observed in the S-wave velocity model as well (Supplementary Fig. S14).

In the intermediate profile (Fig. 6b), both high-velocity anomalies are clearly defined. The Western Alps anomaly is predominantly located at depths of 200–400 km. It likely represents the southward continuation of the Western Alps slab, thinning towards the Earth's surface. The Apenninic high-velocity anomaly is found to the east of the Western Alps slab, at depths of 100–300 km.

In the southernmost profile (Fig. 6c), the shallow portion of the Western Alps slab is no longer visible, as it is replaced by a prominent low-velocity anomaly (L1). Remnants of the high-velocity anomaly remain at depths of 300–400 km. This indicates the southern tip of the Western Alps slab, extending to at least 44°N in map view. The Apenninic slab, in contrast, is visible from the uppermost mantle to depths of 300 km in the southernmost profile. This observation is consistent well with the previously observed NE-dipping subduction of the Apenninic slab in Fig. 3c, providing further support to the hypothesis of an interaction between slabs in the Alps-Apennines transition zone.

3.3. *Eastern Alps - Dinarides transition zone*

Fig. 7 illustrates four SSW-NNE profiles across the complex slab structure beneath the transition zone between the Eastern Alps and the Dinarides. The first and westernmost profile (Fig. 7a) lies to the west of the Giudicarie Line and exclusively intersects the SE-dipping Central Alps slab.

The second profile (Fig. 7b) is situated east of the Giudicarie Line. It crosses a north-dipping high-velocity anomaly, which marks the Eastern Alps slab subducting northward into the mantle transition zone. Beneath the Po Plain, the Central Alps slab remains identifiable, with the low-velocity anomaly L2 situated above it. Along the third profile (Fig. 7c), the north-dipping high-velocity anomaly extends continuously into the mantle transition zone, reaching depths around 600 km. However, this high-velocity anomaly beneath the Eastern Alps is over 300 km wide, suggesting the combined interference of both the Eastern Alps and Dinaric slabs. Although no distinct velocity gap separates the two slabs, the Eastern Alps slab is likely located to the north, and the Dinaric slab is positioned to the south. In the fourth and easternmost profile, the high-velocity anomaly descends deeply into the mantle transition zone, and the Eastern Alps slab appears detached between 130 and 230 km depth as a result of partial horizontal tearing. The Dinaric slab shows no signs of detachment, but the corresponding high-velocity anomaly remains relatively narrow, suggesting that the slab may still be intact, hanging on at greater depths.

4. Discussion

4.1. *Resolution analysis of slab interaction*

To assess the model's capacity to resolve gaps between slabs, we conducted synthetic tests by introducing two subducting slabs in both the Western and Eastern Alps (Fig. 8 and S16). The slabs were modeled as cylinders: in the W1-W1′ cross-section (Fig. 8b), the Western Alps slab dips southeastward at an azimuth of 100°, with a radius of 60 km, while the adjacent Apenninic slab dips northeastward at an azimuth of 40°, with a radius of 50 km. Due to discretization, the slab model presents jagged boundaries. Similarly, in the E3-E3' cross-section, both the Eastern Alps and Dinarides slabs were modeled with a radius of 50 km, dipping at an azimuth of 10° High-velocity anomalies of 3 % and 5 % were assigned to the P-wave and S-wave velocity models, respectively, and a 10 % Gaussian white noise was added to the synthetic relative traveltime residuals to simulate high-level noise. Using the same inversion approach, the recovered velocity models were obtained (Fig. 8 and Supplementary Fig. S16). In the recovered models, the amplitude of the velocity anomalies is reduced, and vertical smearing is observed. Nevertheless, the dip directions of the slabs are well-resolved, and the separation between the Western Alps and Apenninic slabs is also clearly discernible upon visual inspection.

4.2. *Comparison with previous tomography models and seismic anisotropy data*

The complex slab structure beneath the greater Alpine region has been extensively studied over the past decades, with ongoing debates regarding the location and timing of inferred slab breakoff and subduction polarity reversal (e.g., Kissling, 1993; Solarino et al., 1996; Lippitsch et al., 2003; Piromallo and Morelli, 2003; Koulakov et al., 2009; Giacomuzzi et al., 2011, 2012; Zhu et al., 2015; Zhao et al., 2016a; Hua et al., 2017; Sun et al., 2019; El-Sharkawy et al., 2020; Kästle et al., 2020; Zhao et al., 2020; Paffrath et al., 2021; Kästle et al., 2022; Rappisi et al., 2022, 2025). A comparison between our results and the recent ray-based P-wave tomography from Paffrath et al. (2021), which incorporates data from over 600 seismic stations including the AlpArray Seismic Network (Hetenyi et al., 2018), reveals a largely consistent structure of high- and low-velocity anomalies at depths of 150–400 km (Supplementary Fig. S13). For instance, both Paffrath et al. (2021)'s and our models reveal a high-velocity anomaly approximately 300 km wide along the A-A' cross-section (Fig. 3a). The main discrepancies between the two models are observed at the uppermost 150 km, likely due to differences in the crustal correction models used, as well as at depths exceeding 400 km. Notably, Paffrath et al. (2021) incorporated earthquakes with epicentral distances ranging from 35° to 135°, thereby improving ray coverage at greater depths. In contrast, our study utilized earthquakes with epicentral distances between 30° and 90°, deliberately excluding data beyond 90° to mitigate arrival-time anomalies associated with potential heterogeneities in the Earth's core. This key difference in data selection, particularly in the 90°–135° range, likely contributes to the discrepancies observed at depths exceeding 400 km. The continuous slab structure documented in our study, extending from the crust-mantle boundary down to at least 400 km depth, beneath the Alps and the Apennines, aligns with the conclusions recently provided for the Alps by Kästle et al. (2025), who utilized a reversible-jump Markov chain Monte Carlo approach to simultaneously constrain the P and S wave velocity structure and their uncertainties in the crust and upper mantle.

However, when compared to previous studies, our tomography models additionally provide evidence of strong interference between the several slabs imaged beneath the greater Alpine region (see the 3D P-wave velocity model in Supplementary file S2). Slab interaction likely conditioned the mantle flow. For example, the upper mantle beneath the Po Plain appears to be trapped between the Alpine, Dinaric and Apenninic slabs, and therefore is not free to move in a toroidal flow, from the rear to the frontal side of the Apennine slab as a response to Apenninic slab retreat, contrary to the model proposed by Vignaroli et al. (2008). In that region, our S-wave tomography model shows a prominent low-velocity anomaly between 175 and 300 km depth (Fig. 5a), consistent with previous studies supporting the presence of carbon-rich melts in the asthenospheric mantle beneath the Po Plain (Malusà et al., 2018, 2022). These melts are generated when the slab is progressively thermally re-equilibrated toward ambient mantle conditions after cold subduction. Thermal re-equilibration promotes dehydration reactions and carbonate breakdown, with consequent generation of carbon-rich supercritical fluids along the slab interface, which are more easily concentrated in mantle regions with limited active flow (Malusà et al., 2018).

Crucial insights to understand the mantle flow pattern around the interacting slabs of the greater Alpine region is provided by seismic anisotropy data from low-velocity regions (Barruol et al., 2004; Petrescu et al., 2020; Pondrelli et al., 2024), whereas high-velocity regions could include fossil anisotropic fabrics from within the slabs (Plomerová et al., 2006; Salimbeni et al., 2018; Malusà et al., 2021). Recent studies have revealed variations in the direction and strength of seismic anisotropy at varying depths (Hua et al., 2017; Rappisi et al., 2022; Baccheschi et al., 2024) and have provided evidence for inclined anisotropy (Baccheschi et al., 2024).

Given the potential mutual influences between seismic anisotropy and velocity parameters, we have superimposed seismic anisotropy data from different layers onto our S-wave velocity model (Fig. 9), along with dipping anisotropy from splitting intensity (SI) measurements of SKS waves (dt_2 values in Fig. 9a) (Baccheschi et al., 2024). These latter values vary between $dt_2 = 0$, which means horizontal anisotropy, and $dt_2 = 1$, which means inclined anisotropy with dip angle ranging from 30° to 60° (Chevrot, 2000).

Fossil fabrics acquired during Tethyan rifting and preserved in the lithospheric mantle of the Alpine and Apenninic slabs should be marked by slab-parallel to oblique fast axis directions, which are indeed observed, with moderate to high strength, in Fig. 9b-d (see Malusà et al. 2021, for a more in-depth discussion on this topic). The strength of seismic anisotropy is minimal at the junction between the two slabs,

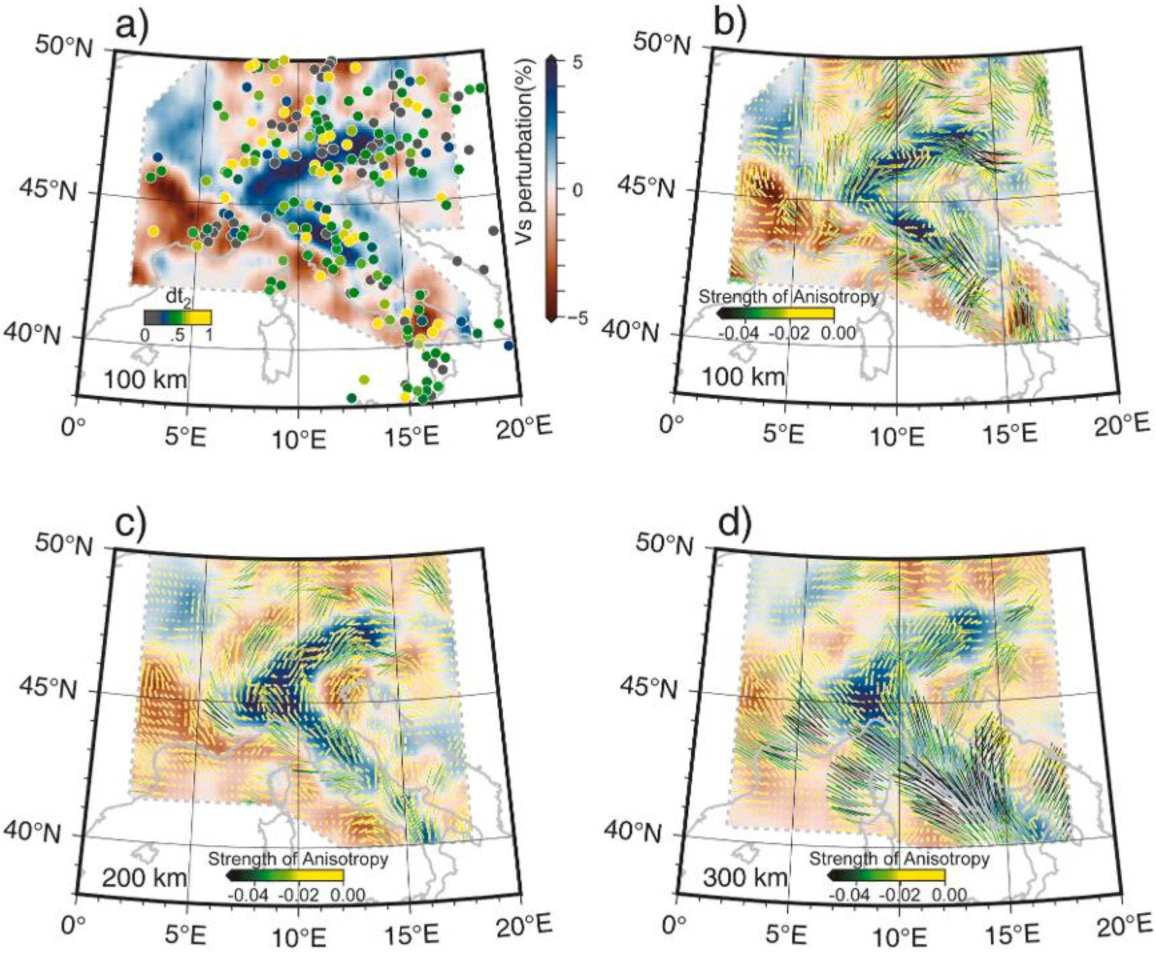

Fig. 9. Relationships between S-wave velocity anomalies and seismic anisotropy. (a) S-wave velocity perturbation at 100 km depth (this work) and dt_2 values (color-coded circles, from Baccheschi et al., 2024) which is a theoretical indicator for inclined anisotropy (gray = horizontal; yellow = 60° dip). **(b-d)** S-wave velocity anomalies (this work) and shear wave anisotropy at 100, 200 and 300 km depth (the length of the color-coded bars is proportional to the modulus of shear wave anisotropy, from Baccheschi et al., 2024).

probably due to internal deformation superimposing the original fossil fabrics (Fig. 9b-d). In the broader region of low-velocity L1 to the west of the Alps, dt_2 values progressively decrease from the west to the east (Fig. 9a). These values suggest a steeply inclined NW-SE anisotropy in southern France, which becomes progressively less inclined eastward and then horizontal near the Alps-Apennines transition zone, where it still preserves a NW-SE orientation (Fig. 9a, b). Anisotropy is evidently deflected at 200 km depth around the southern tip of the Western Alps slab (Fig. 9c) and becomes even more evidently NW-SE oriented and stronger at 300 km depth (Fig. 9d). Beneath the Po Plain, the low-velocity anomaly L2 is associated with weaker anisotropy (yellow colors in Fig. 9b-d). This anisotropy displays NE-SW orientations (Fig. 9b, c) and includes a significant vertical component (Fig. 9a). Stronger azimuthal anisotropy with NE-SW direction is found in the 300 km depth range beneath the entire Adriatic microplate, not only in correspondence with anomaly L2, but also in correspondence with anomaly L3 (Fig. 9d). It aligns well with the NE-SW direction of relative Adria-Europe plate motion inferred from magnetic anomalies since the Late Cretaceous (Dewey et al., 1989; Jolivet and Faccenna, 2000). According to some authors, this anisotropic fabric may have formed during the retreat of the Apenninic slab (e.g., Jolivet et al., 2009), whereas other authors suggest that it may have formed during post-Jurassic Adria-Europe convergence before the onset of slab rollback (e.g., Bacceschi et al., 2024).

Near the base of the Apenninic slab at 200 km depth (Fig. 9c), anisotropy directions within the anomaly L3 are oriented N-S and are invariably associated with a vertical component (Fig. 9a). To the west of the Apenninic slab, in correspondence with anomaly L4, seismic anisotropy is slab parallel and horizontal to slightly inclined, which may suggest a toroidal flow in combination with the directions observed

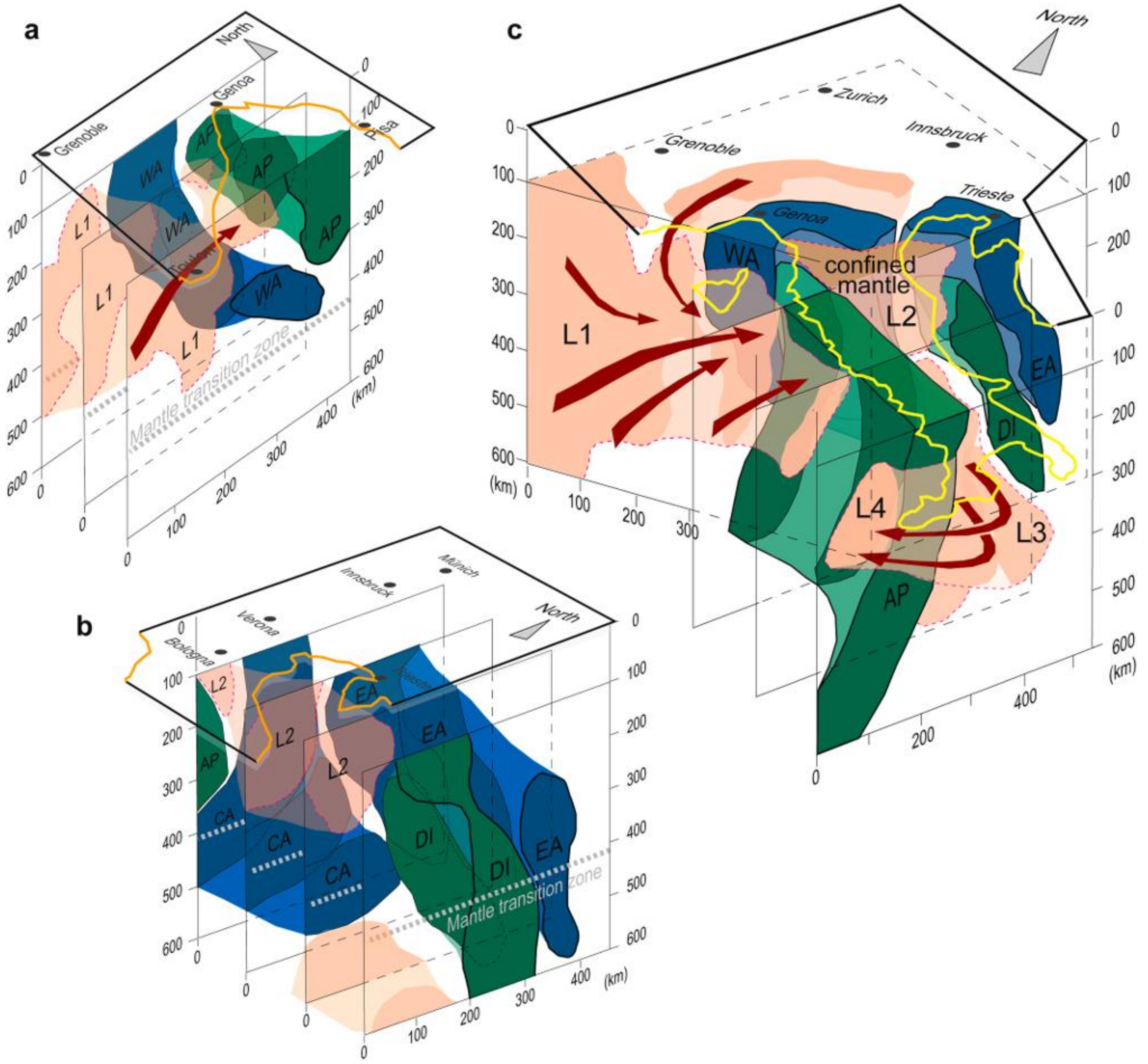

Fig. 10. 3-D interpretive models of slab interference and mantle flow beneath the great Alpine region. (a) Interference between the Apenninic slab and the Western Alps slab based on the cross-sections in Fig. 6. **(b)** Interference between the Dinaric slab and the Central and Eastern Alps slabs based on the cross-sections in Fig. 7. **(c)** Mantle flows (red arrows) around the slabs beneath the greater Alpine region based on cross-sections in Figs. 3 and 5. L1-L4 indicate the main low-velocity anomalies in the mantle. Slabs: AP = Apennines; CA = Central Alps; DI = Dinarides; EA = Eastern Alps; WA = Western Alps.

within anomaly L3. A horizontal and slab-perpendicular anisotropy direction is instead observed at 100 km depth in the central Apennines (Fig. 9a-b), which is supportive of the presence of a slab gap right in the place where the P-wave velocity model reveals a reduction in high-velocity anomaly amplitude (Fig. 2a, b), and the S-wave velocity model exhibits a low-velocity anomaly (Fig. 9a).

4.3. *Relations between slab interaction and mantle flow*

The interaction among the Alpine, Apenninic, and Dinaric slabs, as well as the surrounding mantle flow inferred from tomography and seismic anisotropy, is synthesized in the 3-D interpretive models presented in Fig. 10. Slab interaction is a direct consequence of the prolonged northward motion of the Adriatic microplate relative to Europe since the Late Cretaceous (Dewey et al., 1989; Jolivet and Faccenna, 2000) (Fig. 1a). Previous studies suggested that potential interaction between the Alpine and Apenninic slabs could have controlled the position of the northern tip of the fan-shaped Ligurian-Provençal basin (Malusà et al., 2016). Similarly, interactions between the Alpine and Dinaric slabs may have contributed to the tearing of the Alpine slab, thereby influencing the composition of Eocene-Oligocene magmatic rocks emplaced near the Giudicare Line (Ji et al., 2019; Mosconi et al., 2024).

In the Alps-Apennines transition zone, slab interaction is now evidenced by high-resolution tomography data. As shown in Fig. 10a, a continuous connection is observed between the two slabs. The asthenospheric mantle L2 beneath the Adriatic plate in the Po Plain is not directly connected to the asthenospheric mantle L1 at the rear of the Alpine slab. In the region of slab interaction, the uppermost part of the SW-dipping Apenninic slab is deformed and becomes NE-dipping (Fig. 10c). It has long been recognized that the Apenninic slab underwent retreat in the Neogene, during its northward motion. Slab retreat is expected to induce toroidal flow, displacing part of the underlying mantle from the rear to the front of the retreating slab (Vignaroli et al., 2008; Faccenna and Becker, 2010). However, toroidal flow cannot occur in the absence of a suitable slab gap. Note that the lack of a slab gap would not, in principle, preclude flow pushing the Western Alps slab westward, which would be even more efficient in the presence of a continuous slab as revealed by our finite-frequency tomography model. A westward retreat of the Western Alps slab due to mantle flow pushing should produce, if large enough, a strong E-W seismic anisotropy east of the slab. Such anisotropy is not observed in the L2 anomaly, an observation that could reflect a very small finite westward motion of the Alpine slab, thus making further investigation necessary to better evaluate the different hypotheses.

According to previous studies (Zhao et al., 2016a; Malusà et al., 2021), the absence of a toroidal flow around the northern tip of the retreating Apenninic slab implies that adequate mass compensation is necessarily achieved by the activation of an asthenospheric counterflow to the west of the Alps (red arrow in Fig. 10a). Such counterflow, long recognized based on seismic anisotropy data (e.g., Barruol et al., 2004; Jolivet et al., 2009; Salimbeni et al., 2018), is also expected to involve asthenospheric upwelling to compensate for the lack of mantle material transferred from the rear to the front of the Apenninic slab (Malusà et al., 2021). The inferred vertical component of the counterflow is confirmed by dt_2 values measured to the west of the Alps (Baccheschi et al., 2024) (Fig. 9a), indicating a steeply inclined anisotropy in southern France that becomes progressively less inclined eastward and then horizontal in front of the Apenninic slab (Fig. 10a). The mantle upwelling associated with the counterflow is expected to produce a temperature increase in the upper mantle, potentially explaining the observed low-velocity anomaly L1 observed both in P- and S-wave tomography models.

Slab interaction is also evident in the Eastern Alps – Dinarides transition zone (Fig. 10b). Our tomography models reveal that the northward push of the NE-dipping Dinaric slab against the SE-dipping Alpine slab resulted in a vertical tear in the Alpine slab during the Cenozoic, which became overturned and N-dipping beneath the Eastern Alps. Slab tearing facilitated the ascent of asthenospheric material, as evidenced by the presence of a juvenile component in magmatic rocks exposed in the region between the Giudicarie Line and the Veneto Volcanic Province (Ji et al., 2019; Mosconi et al., 2024). However, any potential connection between the asthenospheric mantle located beneath the Po Plain and the asthenospheric mantle located to the north of the Alpine slab remains limited (Fig. 10b). The asthenospheric mantle corresponding to the low-velocity anomaly L2 is sandwiched between the Central Alps slab below and the northern tip of the Adriatic microplate above, and is laterally confined by the Western Alps slab, by the Dinaric slab and by the Apenninic slab (Fig. 10c), with only possible escape towards the SE. In the S-wave tomography model of Fig. 5, the low-velocity anomaly is stronger between 175 and 300 km depth (Fig. 5b), and according to the higher resolution P-wave tomographic model of Fig. 3b, it is closely associated with the underlying Central Alps slab. These observations support the hypothesis that the low-velocity anomaly L2 may result from carbon-rich melts in the asthenosphere, generated by the breakdown of slab carbonates and hydrous minerals dragged at depth by the cold Alpine subduction (Malusà et al., 2018, 2022). The low-velocity anomalies L1 and L2, located on either side of the Alpine slab may thus have different origins: L1 likely reflects asthenospheric upwelling to the west, whereas L2 is associated with fluids released from the Alpine slab to the east beneath the Po Plain (Malusà et al., 2021). Further south, toroidal flow may still occur around the Apenninic slab, in regions where the mantle flow is not controlled by interference between slabs (L3-L4 Fig. 10).

5. Conclusion

The analysis of a high-resolution P-wave velocity model and a new S-wave velocity model reveals the interactions between the several slabs imaged beneath the greater Alpine region, as well as their relationships with prominent low-velocity anomalies in the upper mantle and associated mantle flow. High-velocity anomalies are identified beneath the Alps, the Apennines and the northern Dinarides. Prominent low-velocity anomalies are observed to the west of the Alps, beneath the Po Plain, and on either side of the central-southern Apennines.

Beneath the Alps-Apennines transition zone, a velocity gap is observed between the interacting Western Alps and Apenninic slabs. The uppermost part of the SW-dipping Apenninic slab is deformed, becoming NE-dipping as a result of slab interaction. The asthenospheric mantle at the rear of the Alpine slab does not directly connect with the asthenospheric mantle beneath the Po Plain. This makes a potential toroidal flow around the northern tip of the retreating Apenninic slab more difficult. As a result, an asthenospheric counterflow may be activated to the west of the Alps to compensate for the lack of mantle material transferred from the rear to the front of the Apenninic slab. Such a counterflow may include a component of asthenospheric upwelling that produces a temperature increase in the upper mantle with consequent decrease in P- and S-wave velocities, a working hypothesis that is worth exploring further.

Beneath the Eastern Alps, the NE-dipping Dinaric slab is pushed against the Alpine slab, which has been torn and overturned to become N-dipping. Despite slab tearing, no significant connection is observed between the asthenospheric mantle located to the north of the Alpine slab and the asthenospheric mantle located beneath the Po Plain, which is confined by slabs and remains unaffected by major mantle flow. The presence of a prominent low-velocity anomaly in that region, closely associated with the underlying Central Alps slab, supports the hypothesis that the generation of carbon-rich supercritical fluids at the top of the slab triggered melting in the overlying mantle wedge, resulting in a decrease in seismic velocities. Toroidal flow is likely to occur farther south around the Apenninic slab, in a region where the mantle flow is not controlled by slab interactions.

We conclude that, because of slab interference, low-velocity anomalies of different origin, either due to asthenospheric upwelling or slab fluids, may coexist in nearby regions of the upper mantle, with major implications for dynamic numerical modeling applied to the analysis of sub-lithospheric mantle convection (e.g., Faccenna and Becker, 2010; Sternai et al., 2019). Our findings may also be relevant for interpretating mantle processed in other complex plate-boundary zones, such as the Taiwan orogeny (Byrne and Liu, 2002) or the Hindu Kush - Pamir - Tianshan tectonic knot in Central Asia (Kufner et al., 2016; Sun et al., 2022), where a complex interplay between opposite-dipping slabs is revealed by geophysical and geological data.

Data availability

Seismic data of the China-Italy-France Alps seismic transects CIFALPS (Zhao et el. 2016b: https://www.fdsn.org/networks/detail/YP_2012/) and CIFALPS2 (Zhao et el. 2018: https://www.fdsn.org/networks/detail/XT_2018/) temporary experiments are distributed by the datacenter of the French geodetic and seismological network RESIF, and by the IGGCAS datacenter (Institute of Geology and Geophysics, Chinese Academy of Sciences). The AlpArray temporary seismic data are available on EIDA (https://www.fdsn.org/networks/detail/Z3_2015/). We also used records of permanent networks available on EIDA (http://eida.gfz.de/webdc3/).

CRediT authorship contribution statement

Yuantong Mao: Writing – original draft, Visualization, Methodology, Data curation. **Xiaotian Tang:** Data curation. **Liang Zhao:** Writing – review & editing, Validation, Supervision, Funding acquisition, Conceptualization. **Marco G. Malusà:** Writing – review & editing, Visualization, Investigation, Formal analysis. **Stéphane Guillot:** Writing – review & editing, Formal analysis, Conceptualization. **Anne Paul:** Writing – review & editing. **Stefano Solarino:** Writing – review & editing. **Xiaobing Xu:** Writing – review & editing, Data curation. **Coralie Aubert:** Writing – review & editing. **Elena Eva:** Writing – review & editing. **Silvia Pondrelli:** Writing – review & editing. **Simone Salimbeni:** Writing – review & editing. **Lei Yang:** Writing – review & editing.

Declaration of competing interest

The authors declare that they have no known competing financial interests or personal relationships that could have appeared to influence the work reported in this paper.

Acknowledgments

This work was supported by the National Natural Science Foundation of China (Grants 92355001, 42488201). We would like to express our sincere respect and gratitude to CIFALPS team and ALPARRAY group for providing the valuable seismic data used in this study. The authors are grateful to the operators of European permanent seismic networks who make their data available through EIDA (http://www. orfeus-eu.org/data/eida/). Our thanks also go to Nouibat et al. (2022, 2023) for sharing their crustal velocity model through the EaSy Data platform (https://doi.org/10.57932/c8babd3b-2781-46e1-b4de-ae874cacb056). We thank Laurent Jolivet and an anonymous reviewer for their insightful comments, which helped us improve the clarity of the manuscript.

Supplementary materials

Supplementary material associated with this article can be found, in the online version, at doi:10.1016/j.epsl.2025.119716.

Data availability

I have shared the link to my data in the manuscript

References

Baccheschi, P., Confal, J.M., Pondrelli, S., 2024. Splitting intensity tomography to image depth-dependent seismic anisotropy patterns beneath the Italian Peninsula and surrounding regions. Earth Planet Sci. Lett. 646, 119005.

Barruol, G., Deschamps, A., Coutant, O., 2004. Mapping upper mantle anisotropy beneath SE France by SKS splitting indicates neogene asthenospheric flow induced by Apenninic slab roll-back and deflected by the deep Alpine roots. Tectonophysics 394, 125–138.

Brocher, T.M., 2005. Empirical relations between elastic wavespeeds and density in the Earth's crust. B. Seism. Soc. Am. 95, 2081–2092.

Byrne, T.B., Liu, C.S. (Eds.), 2002. Geology and Geophysics of an Arc-Continent Collision. Geological Society of America, Taiwan.

Chevrot, S., 2000. Multichannel analysis of shear wave splitting. J. Geophys. Res.: Solid Earth 105, 21579–21590.

Recherches séismologiques dans les Alpes occidentales au moyen de grandes explosions en 1956, 1958 et 1960: mémoire collectif du Groupe d'études des explosions alpines /rédacteurs: H. Closs et Y. Labrouste. In: Closs, H., Labrouste, Y. (Eds.), Recherches séismologiques dans les Alpes occidentales au moyen de grandes explosions en 1956, 1958 et 1960: mémoire collectif du Groupe d'études des explosions alpines /rédacteurs: H. Closs et Y. Labrouste. Cent. Natl. Rech. Sci. [Paris].

Dahlen, F.A., Hung, S.H., Nolet, G., 2000. Fréchet kernels for finite-frequency traveltimes—I. Theory. Geophys. J. Int. 141, 157–174.

Dewey, J.F., Helman, M.L., Knott, S.D., Turco, E., Hutton, D.H.W., 1989. Kinematics of the Western Mediterranean. Geological Society, 45. Special Publications, London, pp. 265–283.

El-Sharkawy, A., Meier, T., Lebedev, S., Behrmann, J.H., Hamada, M., Cristiano, L., Weidle, C., Köhn, D., 2020. The slab puzzle of the Alpine-Mediterranean region: insights from a new, high-resolution, shear wave velocity model of the upper mantle. Geochem. Geophys. Geosyst. 21, e2020GC008993.

Eva, E., Malusà, M.G., Solarino, S., 2020. Seismotectonics at the transition between opposite-dipping slabs (Western Alpine Region). Tectonics 39, e2020TC006086.

Faccenna, C., Becker, T.W., 2010. Shaping mobile belts by small-scale convection. Nature 465, 602–605.

Gattacceca, J., Deino, A., Rizzo, R., Jones, D.S., Henry, B., Beaudoin, B., Vadeboin, F., 2007. Miocene rotation of Sardinia: new paleomagnetic and geochronological constraints and geodynamic implications. Earth Planet Sci. Lett. 258, 359–377.

Giacomuzzi, G., Chiarabba, C., De Gori, P., 2011. Linking the Alps and Apennines subduction systems: new constraints revealed by high-resolution teleseismic tomography. Earth Planet Sci. Lett. 301, 531–543.

Giacomuzzi, G., Civalleri, M., De Gori, P., Chiarabba, C., 2012. A 3D vs model of the upper mantle beneath Italy: insight on the geodynamics of central Mediterranean. Earth Planet Sci. Lett. 335-336, 105–120.

E. Handy, M.R., Schmid, M., Bousquet, S., Kissling, R., Bernoulli, D., 2010. Reconciling plate-tectonic reconstructions of Alpine Tethys with the geological–geophysical record of spreading and subduction in the Alps Earth-Sci. Rev. 102, 121–158.

Hetenyi, G., Molinari, I., Clinton, J., Bokelmann, G., Bondar, I., Crawford, W.C., Dessa, J. X., Doubre, C., Friederich, W., Fuchs, F., Giardini, D., Graczer, Z., Handy, M.R., Herak, M., Jia, Y., Kissling, E., Kopp, H., Korn, M., Margheriti, L., Meier, T., Mucciarelli, M., Paul, A., Pesaresi, D., Piromallo, C., Plenefisch, T., Plomerova, J., Ritter, J., Rumpker, G., Sipka, V., Spallarossa, D., Thomas, C., Tilmann, F., Wassermann, J., Weber, M., Weber, Z., Wesztergom, V., Zivcic, M., 2018. The AlpArray seismic network: a large-scale European experiment to image the alpine orogen. Surv. Geophys. 39, 1009–1033.

Hua, Y., Zhao, D., Xu, Y., 2017. P wave anisotropic tomography of the Alps. J. Geophys. Res.: Solid Earth 122, 4509–4528.

Hung, S.H., Dahlen, F.A., Nolet, G., 2000. Fréchet kernels for finite-frequency traveltimes-II. Ex. Geophys J. Int. 141, 175–203.

Ji, W.Q., Malusà, M.G., Tiepolo, M., Langone, A., Zhao, L., Wu, F.Y., 2019. Synchronous Periadriatic magmatism in the Western and Central Alps in the absence of slab breakoff. Terra Nova 31, 120–128.

Jolivet, L., Faccenna, C., 2000. Mediterranean extension and the Africa-Eurasia collision. Tectonics 19, 1095–1106.

Jolivet, L., Faccenna, C., Piromallo, C., 2009. From mantle to crust: stretching the Mediterranean. Earth Planet Sci. Lett. 285, 198–209.

Jozi Najafabadi, A., Haberland, C., Le Breton, E., Handy, M.R., Verwater, V.F., Heit, B., Weber, M., 2022. Constraints on crustal structure in the vicinity of the adriatic indenter (European Alps) from vp and vp/vs local earthquake tomography. J. Geophys. Res.: Solid Earth 127 e2021JB023160.

Kästle, E.D., El-Sharkawy, A., Boschi, L., Cristiano, L., Weidle, C., 2018. SurfaceWave tomography of the Alps using ambient-noise and earthquake phase velocity measurements. J. Geophys Res.: Solid Earth 123, 1770–1792.

Kästle, E.D., Molinari, I., Boschi, L., Kissling, E., 2022. Azimuthal anisotropy from eikonal tomography: example from ambient-noise measurements in the AlpArray network. Geophys. J. Int. 229, 151–170.

Kästle, E.D., Paffrath, M., El-Sharkawy, A., 2025. Alpine crust and mantle structure from 3D Monte Carlo surfaceand body-wave tomography. J. Geophys. Res.: Solid Earth 130 e2024JB030101.

Kästle, E.D., Rosenberg, C., Boschi, L., Bellahsen, N., Meier, T., El-Sharkawy, A., 2020. Slab break-offs in the Alpine subduction zone. Int. J. Earth Sci. 109, 587–603.

Kennett, B.L.N., Engdahl, E.R., 1991. Traveltimes for global earthquake location and phase identification. Geophys. J. Int. 105, 429–465.

Kind, R., Schmid, S.M., Schneider, F., Meier, T., Yuan, X., Heit, B., Schiffer, C., 2023. Sp converted waves reveal the structure of the lithosphere below the Alps and their northern foreland. Geophys. J. Int 235, 1832–1848.

Kissling, E., 1993. Deep structure of the Alps—What do we really know? Phys. Earth Planet. In. 79, 87–112.

Koulakov, I., Kaban, M.K., Tesauro, M., Cloetingh, S., 2009. P- andS-velocity anomalies in the upper mantle beneath Europe from tomographic inversion of ISC data. Geophys. J. Int. 179, 345–366.

Kufner, S.-K., Schurr, B., Sippl, C., Yuan, X., Ratschbacher, L., Akbar, A.s.o.M., Ischuk, A., Murodkulov, S., Schneider, F., Mechie, J., Tilmann, F., 2016. Deep India meets deep Asia: lithospheric indentation, delamination and break-off under Pamir and Hindu Kush (Central Asia). Earth Planet Sci. Lett. 435, 171–184.

Lévêque, J.-J., Rivera, L., Wittlinger, G., 1993. On the use of the checker-board test to assess the resolution of tomographic inversions. Geophys. J. Int. 115, 313–318.

Lippitsch, R., Kissling, E., Ansorge, J., 2003. Upper mantle structure beneath the Alpine orogen from high-resolution teleseismic tomography. J. Geophys. Res. 108, 2376.

Lu, Y., Stehly, L., Brossier, R., Paul, A., Group, A.W., 2020. Imaging Alpine crust using ambient noise wave-equation tomography. Geophys. J. Int. 222, 69–85.

Malusà, M.G., Anfinson, O.A., Dafov, L.N., Stockli, D.F., 2016. Tracking Adria indentation beneath the Alps by detrital zircon U-Pb geochronology: implications for the oligocene–Miocene dynamics of the adriatic microplate. Geology 44, 155–158.

Malusà, M.G., Brandmayr, E., Panza, G.F., Romanelli, F., Ferrando, S., Frezzotti, M.L., 2022. An explosive component in a December 2020 Milan earthquake suggests outgassing of deeply recycled carbon. Commun. Earth Env. 3, 5.

Malusà, M.G., Faccenna, C., Baldwin, S.L., Fitzgerald, P.G., Rossetti, F., Balestrieri, M.L., Danišík, M., Ellero, A., Ottria, G., Piromallo, C., 2015. Contrasting styles of (U)HP rock exhumation along the cenozoic Adria-Europe plate boundary (Western Alps, Calabria, Corsica). Geochem. Geophys. Geosyst. 16, 1786–1824.

Malusa, M.G., Frezzotti, M.L., Ferrando, S., Brandmayr, E., Romanelli, F., Panza, G.F., 2018. Active carbon sequestration in the Alpine mantle wedge and implications for long-term climate trends. Sci. Rep. 8, 4740.

Malusà, M.G., Guillot, S., Zhao, L., Paul, A., Solarino, S., Dumont, T., Schwartz, S., Aubert, C., Baccheschi, P., Eva, E., Lu, Y., Lyu, C., Agostinetti, N.P., Pondrelli, S., Salimbeni, S., Sun, W., Yuan, H., 2021. The deep structure of the Alps based on the CIFALPS seismic experiment: a synthesis. Geochem. Geophys. Geosyst. 22, e2020GC009466.

Mao, Y., Zhao, L., Malusà, M.G., Solarino, S., Pondrelli, S., Sun, B., Aubert, C., Salimbeni, S., Eva, E., Guillot, S., 2024. Geophysical evidence of large-scale silica-rich fluid flow above the continental subduction interface. Sci. China Earth Sci. 67, 2796–2809.

Monna, S., Montuori, C., Frugoni, F., Piromallo, C., Vinnik, L., 2022. Moho and LAB across the Western Alps (Europe) from P and S receiver function analysis. J. Geophys. Res.: Solid Earth 127, e2022JB025141.

Mosconi, A., Cannaò, E., Farina, F., Malusà, M.G., Zanchetta, S., Tiepolo, M., 2024. The Corno Alto complex (Adamello batholith): a modern analogue of the high Ba/K sanukitoids. Lithos 470–471.

Nouibat, A., Brossier, R., Stehly, L., Cao, J., Paul, A., 2023. Ambient-noise wave-equation tomography of the Alps and Ligurian-Provence Basin. J. Geophys. Res.: Solid Earth 128.

Nouibat, A., Stehly, L., Paul, A., Schwartz, S., Bodin, T., Dumont, T., Rolland, Y., Brossier, R., 2022. Lithospheric transdimensional ambient-noise tomography of W-Europe: implications for crustal-scale geometry of the W-Alps. Geophys. J. Int. 229, 862–879.

Paffrath, M., Friederich, W., Schmid, S.M., Handy, M.R., 2021. Imaging structure and geometry of slabs in the greater Alpine area – a P-wave travel-time tomography using AlpArray Seismic Network data. Solid Earth 12, 2671–2702.

Paige, C.C., Saunders, M.A., 1982. LSQR: an algorithm for sparse linear equations and sparse least squares. ACM Trans. Math. Softw. 8, 43–71.

Paul, A., Malusà, M.G., Solarino, S., Salimbeni, S., Eva, E., Nouibat, A., Pondrelli, S., Aubert, C., Dumont, T., Guillot, S., Schwartz, S., Zhao, L., 2022. Along-strike variations in the fossil subduction zone of the Western Alps revealed by the CIFALPS seismic experiments and their implications for exhumation of (ultra-) high-pressure rocks. Earth Planet Sci. Lett. 598, 117843.

Petrescu, L., Pondrelli, S., Salimbeni, S., Faccenda, M., 2020. Mantle flow below the central and greater Alpine region: insights from SKS anisotropy analysis at AlpArray and permanent stations. Solid Earth 11, 1275–1290.

Piromallo, C., Morelli, A., 2003. P wave tomography of the mantle under the Alpine-Mediterranean area. J. Geophys. Res. 108, 2065.

Plomerova, J., Margheriti, L., Park, J., Babuska, V., Pondrelli, S., Vecsey, L., Piccinini, D., Levin, V., Baccheschi, P., Salimbeni, S., 2006. Seismic anisotropy beneath the Northern Apennines (Italy): mantle flow or lithosphere fabric? Earth Planet Sci. Lett. 247, 157–170.

Pondrelli, S., Salimbeni, S., Confal, J.M., Malusà, M.G., Paul, A., Guillot, S., Solarino, S., Eva, E., Aubert, C., Zhao, L., 2024. Highlights on mantle deformation beneath the Western Alps with seismic anisotropy using CIFALPS2 data. Solid Earth 15, 827–835.

Rappisi, F., VanderBeek, B.P., Faccenda, M., Morelli, A., Molinari, I., 2022. Slab geometry and upper mantle flow patterns in the Central Mediterranean from 3D anisotropic P-wave tomography. J. Geophys Res.: Solid Earth 127, e2021JB023488.

Rawlinson, N., Sambridge, M., 2003. Seismic traveltime tomography of the crust and lithosphere. Adv. Geophys. 46, 81–197.

Salimbeni, S., Malusà, M.G., Zhao, L., Guillot, S., Pondrelli, S., Margheriti, L., Paul, A., Solarino, S., Aubert, C., Dumont, T., Schwartz, S., Wang, Q., Xu, X., Zheng, T., Zhu, R., 2018. Active and fossil mantle flows in the western Alpine region unravelled by seismic anisotropy analysis and high-resolution P wave tomography. Tectonophysics 731-732, 35–47.

Solarino, S., Malusà, M.G., Eva, E., Guillot, S., Paul, A., Schwartz, S., Zhao, L., Aubert, C., Dumont, T., Pondrelli, S., Salimbeni, S., Wang, Q., Xu, X., Zheng, T., Zhu, R., 2018. Mantle wedge exhumation beneath the Dora-Maira (U)HP dome unravelled by local earthquake tomography (Western Alps). Lithos 296-299, 623–636.

Solarino, S., Malusà, M.G., Eva, E., Paul, A., Guillot, S., Pondrelli, S., Salimbeni, S., Zhao, L., 2024. Seismic tomography reveals contrasting styles of subduction-channel and mantle-wedge exhumation controlled by upper plate divergent motion. Gondwana Res. 136, 169–182.

Solarino, S., Spallarossa, D., Parolai, S., Cattaneo, M., Eva, C., 1996. Litho—Asthenospheric structures of northern Italy as inferred from teleseismic P-wave tomography. Tectonophysics 260, 271–289.

Sternai, P., Sue, C., Husson, L., Serpelloni, E., Becker, T.W., Willett, S.D., Faccenna, C., Di Giulio, A., Spada, G., Jolivet, L., Valla, P., Petit, C., Nocquet, J.-M., Walpersdorf, A., Castelltort, S., 2019. Present-day uplift of the European Alps: evaluating mechanisms and models of their relative contributions. Earth-Sci. Rev. 190, 589–604.

Sun, W., Ao, S., Tang, Q., Malusà, M.G., Zhao, L., Xiao, W., 2022. Forced cenozoic continental subduction of Tarim craton-like lithosphere below the Tianshan revealed by ambient noise tomography. Geology. 50, 1393–1397.

Sun, W., Zhao, L., Malusà, M.G., Guillot, S., Fu, L., 2019. 3-D pn tomography reveals continental subduction at the boundaries of the Adriatic microplate in the absence of a precursor oceanic slab. Earth Planet Sci. Lett. 510, 131–141.

VanDecar, J.C., Crosson, R.S., 1990. Determination of teleseismic relative phase arrival times using multi-channel cross-correlation and least squares. B. Seism. Soc. Am. 80, 150–169.

Vignaroli, G., Faccenna, C., Jolivet, L., Piromallo, C., Rossetti, F., 2008. Subduction polarity reversal at the junction between the western Alps and the Northern Apennines. Italy. Tectonophys. 450, 34–50.

Yu, C., Zheng, Y., Shang, X., 2017. Crazyseismic: a MATLAB GUI-based software package for passive seismic data preprocessing. Seism. Res. Lett. 88, 410–415.

Zhao, L., Malusà, M.G., Yuan, H., Paul, A., Guillot, S., Lu, Y., Stehly, L., Solarino, S., Eva, E., Lu, G., Bodin, T., 2020. Evidence for a serpentinized plate interface favouring continental subduction. Nat. Commun. 11, 2171.

Zhao, L., Paul, A., Guillot, S., Solarino, S., Malusà, M.G., Zheng, T., Aubert, C., Salimbeni, S., Dumont, T., Schwartz, S., Zhu, R., Wang, Q., 2015. First seismic evidence for continental subduction beneath the Western Alps. Geology 43, 815–818.

Zhao, L., Paul, A., Malusà, M.G., Xu, X., Zheng, T., Solarino, S., Guillot, S., Schwartz, S., Dumont, T., Salimbeni, S., Aubert, C., Pondrelli, S., Wang, Q., Zhu, R., 2016a. Continuity of the Alpine slab unraveled by high-resolution P wave tomography. J. Geophys. Res.: Solid Earth 121, 8720–8737.

Zhao, L., Paul, A., Solarino, S., 2018. Seismic Network XT: CIFALPS2 Temporary Experiment (China-Italy-France Alps seismic Transect #2). RESIF - Réseau Sismologique et géodésique Français. https://doi.org/10.15778/RESIF.XT2018 [/Dataset].

Zhao, L., Paul, A., Stephano, S., 2016b. Seismic Network YP: CIFALPS Temporary Experiment (China-Italy-France Alps seismic Transect). RESIF - Réseau Sismologique et géodésique Français. https://doi.org/10.15778/RESIF.YP2012 [/Dataset].

Zhu, H., Bozdağ, E., Tromp, J., 2015. Seismic structure of the European upper mantle based on adjoint tomography. Geophys. J. Int. 201, 18–52.